

Dartmouth College Dartmouth Digital Commons

Open Dartmouth: Faculty Open Access Articles

2-4-2015

Macroscopic Optical Imaging Technique for Wide-Field Estimation of Fluorescence Depth in Optically Turbid Media for Application in Brain Tumor Surgical Guidance

Kolbein K. Kolste
Dartmouth College

Stephen C. Kanick
Dartmouth College


Pablo A. Valdés
Dartmouth College

Michael Jermyn
Polytechnique Montreal

Brian C. Wilson
Ontario Cancer Institute

See next page for additional authors

Follow this and additional works at: <https://digitalcommons.dartmouth.edu/facoa>

 Part of the [Engineering Commons](#), and the [Medicine and Health Sciences Commons](#)

Recommended Citation

Kolste, Kolbein K.; Kanick, Stephen C.; Valdés, Pablo A.; Jermyn, Michael; Wilson, Brian C.; Roberts, David W.; Paulsen, Keith D.; and Leblond, Frederic, "Macroscopic Optical Imaging Technique for Wide-Field Estimation of Fluorescence Depth in Optically Turbid Media for Application in Brain Tumor Surgical Guidance" (2015). *Open Dartmouth: Faculty Open Access Articles*. 3742.
<https://digitalcommons.dartmouth.edu/facoa/3742>

This Article is brought to you for free and open access by Dartmouth Digital Commons. It has been accepted for inclusion in Open Dartmouth: Faculty Open Access Articles by an authorized administrator of Dartmouth Digital Commons. For more information, please contact dartmouthdigitalcommons@groups.dartmouth.edu.

Authors

Kolbein K. Kolste, Stephen C. Kanick, Pablo A. Valdés, Michael Jermyn, Brian C. Wilson, David W. Roberts, Keith D. Paulsen, and Frederic Leblond

Macroscopic optical imaging technique for wide-field estimation of fluorescence depth in optically turbid media for application in brain tumor surgical guidance

Kolbein K. Kolste
Stephen C. Kanick
Pablo A. Valdés
Michael Jermyn
Brian C. Wilson
David W. Roberts
Keith D. Paulsen
Frederic Leblond

Macroscopic optical imaging technique for wide-field estimation of fluorescence depth in optically turbid media for application in brain tumor surgical guidance

Kolbein K. Kolste,^a Stephen C. Kanick,^a Pablo A. Valdés,^{a,b} Michael Jermyn,^c Brian C. Wilson,^d David W. Roberts,^e Keith D. Paulsen,^a and Frederic Leblond^{c,*}

^aDartmouth College, Thayer School of Engineering, Hanover, 14 Engineering Drive, New Hampshire 03755, United States

^bDartmouth College, Geisel School of Medicine, Hanover, 1 Rope Ferry Road, New Hampshire 03755, United States

^cPolytechnique Montreal, Engineering Physics Department, Montreal, Québec H3C 3A7, Canada

^dUniversity of Toronto, Ontario Cancer Institute, 610 University Avenue, Toronto, Ontario M5G 2M9, Canada

^eDartmouth-Hitchcock Medical Center, Section of Neurosurgery, 1 Medical Center Drive, Lebanon, New Hampshire 03756, United States

Abstract. A diffuse imaging method is presented that enables wide-field estimation of the depth of fluorescent molecular markers in turbid media by quantifying the deformation of the detected fluorescence spectra due to the wavelength-dependent light attenuation by overlying tissue. This is achieved by measuring the ratio of the fluorescence at two wavelengths in combination with normalization techniques based on diffuse reflectance measurements to evaluate tissue attenuation variations for different depths. It is demonstrated that fluorescence topography can be achieved up to a 5 mm depth using a near-infrared dye with millimeter depth accuracy in turbid media having optical properties representative of normal brain tissue. Wide-field depth estimates are made using optical technology integrated onto a commercial surgical microscope, making this approach feasible for real-world applications. © 2015 Society of Photo-Optical Instrumentation Engineers (SPIE) [DOI: 10.1117/1.JBO.20.2.026002]

Keywords: diffuse optics; fluorescence; surgery; spectroscopy; topography; molecular imaging.

Paper 140660R received Oct. 8, 2014; accepted for publication Jan. 5, 2015; published online Feb. 4, 2015.

1 Introduction

Optical techniques such as confocal and two-photon fluorescence microscopy yield micron-resolution images of tissue sections down to depths of a few hundred microns, beyond which multiple light scattering causes significant blurring. For many biomedical applications, particularly *in vivo*, it is often necessary to compromise on the spatial resolution in order to achieve larger fluorescence imaging depths over large (cm-scale) field of view (FOV). One such application is fluorescence-guided cancer surgery, using red/near-infrared (NIR) molecular probes.^{1,2} In the last decade, this approach has been most highly developed for brain tumor surgery using the optical contrast provided by protoporphyrin IX (PpIX) that is endogenously synthesized in tumor cells following administration of the pro-drug δ -aminolevulinic acid (ALA).³⁻⁷ Significant improvement in survival has been demonstrated in patients with high-grade glioma,^{7,8} even using qualitative visual assessment of the PpIX fluorescence to identify residual tumor after white-light resection, and we have previously reported on preclinical and clinical techniques to quantify the absolute PpIX concentration in the tissue at the time of surgery, using either a point probe spectroscopy technique^{6,9-16} or wide-field quantitative imaging of the tissue surface.^{5,17-21} In this and other clinical applications, the ability to detect fluorescent tumor foci lying significantly below the surface of the surgical cavity could further increase

the completeness of tumor resection to impact survival and also improve patient safety by minimizing the need for blind exploratory resection.^{8,22-24} This is the focus of the work reported here.

There is considerable ongoing preclinical development of novel high-specificity, molecularly targeted NIR fluorescent imaging agents that can eventually be translated to clinical use for surgical guidance.²⁵⁻²⁷ The use of NIR fluorophores allows detection of fluorescence from significant depths in tissue due to the relatively low optical absorption above the main hemoglobin absorption range and the reduced scattering at these wavelengths. However, since most tissues are still highly turbid (scattering \gg absorption) at these wavelengths, the rapid diffusion of the light degrades the attainable spatial resolution. In addition, the concentration and depth of the fluorescent sources are difficult to separate: e.g., the same detected signal can be generated from a low fluorophore concentration close to the tissue surface or a high concentration at depth. This is addressed here by introducing a topographic technique to estimate the fluorophore depth. The technique has been specifically developed for ALA-PpIX fluorescence-guided brain cancer surgery, but the concept can be applied to other fluorophores and tumor sites with suitable adjustment of the wavelengths and corresponding tissue optical properties.

Over the last two decades, several approaches have been developed to localize fluorescent sources *in vivo*, especially

*Address all correspondence to: Frederic Leblond, E-mail: frederic.leblond@polymtl.ca

for whole-body preclinical imaging using small animal models (see Ref. 28 for a review). These include diffuse fluorescence tomographic imaging by scanning over multiple source-detector positions, for example by using photon time-of-flight methods implemented in either the time or frequency domain.^{29–32} Other techniques rely on time-resolved single-point detection to retrieve the source depth based on the average photon time of flight.³³ However, data acquisition for these techniques can be time consuming, typically requires expensive equipment, and is very sensitive to small instrument misalignments, making them very difficult to implement for routine surgical guidance in critical sites such as the brain. In neurosurgery, the introduction of novel technologies complementing the standard of care (i.e., neurosurgical microscope and neuronavigation unit) must be minimally disruptive to the surgeon workflow. As a result, instrumentation with a minimal footprint is required that can provide surgeons with optical information within time frames compatible with the flow of a surgical procedure (i.e., within a few seconds). Here, we are presenting such a technique, namely a multispectral, dual wavelength, self-normalized technique that can be seamlessly integrated onto a commercial surgical microscope to provide topographic maps of fluorescent sources down to several millimeters in tissue with ~1 mm accuracy and precision.

By topographic imaging, here we mean that the depth of the fluorescent structure that is closest to the accessible tissue surface (e.g., the resection cavity) is determined. This is distinct from fluorescence tomography where the goal is to reconstruct the full three-dimensional fluorophore distribution in the tissue. We have previously reported two complementary methods of fluorescence topography, as demonstrated using PpIX as the fluorophore. Initially, multiple excitation wavelengths in the visible range were used, with a common long-wavelength detection band (>635 nm).²¹ The effective optical sampling depth (which depends on the wavelength-dependent tissue optical properties) of the fluorophore then primarily depended on the excitation wavelengths. By ordering the resulting fluorescent images according to the increasing penetration depth of the excitation light and applying a threshold value to the signals, a tomographic two-dimensional depth profile was generated that was experimentally shown to represent the top surface of the subsurface fluorophore distribution. The depth accuracy in brain was ± 0.5 mm up to a depth of about 3 mm for PpIX. In the second method,¹⁹ the longest excitation wavelength of PpIX (635 nm) was used and hyperspectral fluorescence images were taken at the tissue surface. The wavelength-dependent distortion of the detected fluorescent light was shown to correlate with the effective depth (up to >1 cm) of the fluorophore and thereby suggested that a tomographic subsurface image could be produced.

The present work develops this second approach further by demonstrating that a simple ratiometric method can be used to actually retrieve the fluorophore depth. The fact that the technique is directly integrated onto a neurosurgical microscope and that image acquisition and processing can be achieved within a few seconds should facilitate its translation to clinical use. In brief, the technique relies on the observation that the logarithm of the ratio, Γ , of the detected fluorescence signal at the tissue surface at two wavelengths varies linearly with the depth, d , of a fluorescent point source in an optically turbid medium, as experimentally demonstrated by Swartling et al.³⁴ Our group previously derived analytic solutions to the diffusion equation

for this situation in order to better understand the physical basis of this relationship.¹⁹ Thus, we showed that for a point-like fluorescent inclusion

$$\ln(\Gamma) = \left(\frac{1}{\delta^{\lambda^2}} - \frac{1}{\delta^{\lambda^1}} \right) \times d + \ln \left(\frac{D^{\lambda^2}}{D^{\lambda^1}} \right), \quad (1)$$

where the tissue optical properties at wavelength, λ , are characterized by the diffusion coefficient

$$D = \frac{1}{3(\mu_a + \mu_s')}, \quad (2)$$

and the effective penetration depth

$$\delta = \sqrt{\frac{D}{\mu_a}}, \quad (3)$$

both of which are functions of the absorption coefficient, μ_a , and the reduced scattering coefficient, μ_s' .³⁵

Equation (1) is of the general form

$$\ln(\Gamma) = m \times d + b, \quad (4)$$

so that we hypothesize that dual-wavelength fluorescence ratio-metric imaging can be used for topographic mapping of the subsurface fluorophore depth from the expression

$$d = \frac{\ln(\Gamma) - b}{m}. \quad (5)$$

Thus, the hypothesis we are making here is that the depth of fluorescent sources can be estimated even in cases where the distribution is not point-like, as explained and motivated in Ref. 19. Clearly, the use of Eq. (5) to retrieve the depth using a wide-field imaging system for every image pixel requires making reliable estimates for m and b . In the present work, we are introducing a normalization technique to make the depth-retrieval independent of the intercept b and where tissue attenuation properties are used to estimate a value for the slope parameter m by applying either light transport models (requiring the tissue optical properties to be known *a priori*) or non-model-based techniques using measured diffuse reflectance data. It is demonstrated that depth estimates can be obtained with $\pm \sim 1$ mm accuracy using Eq. (1) when the optical properties are known *a priori*. Similar depth accuracy can be achieved using a non-model-based approach, but only for a restricted subset of tissue absorption and scattering values. The approach is also limited to high-contrast fluorescent targets, i.e., where the tissue autofluorescence is low relative to the exogenous fluorophore. As we have previously demonstrated, this condition is realized for ALA-PpIX fluorescence for a range of brain tumors, including high-grade glioma and meningioma.¹³

2 Materials and Methods

2.1 Imaging System

Figure 1 shows a schematic of the hyperspectral imaging system, which is attached to a free optical port on a commercial neurosurgical microscope (Carl Zeiss Meditec). The microscope has optics allowing zoom and FOV adjustment and is equipped with a variable-intensity bright-field tungsten-halogen lamp (white light) for surface structural imaging. The design of the

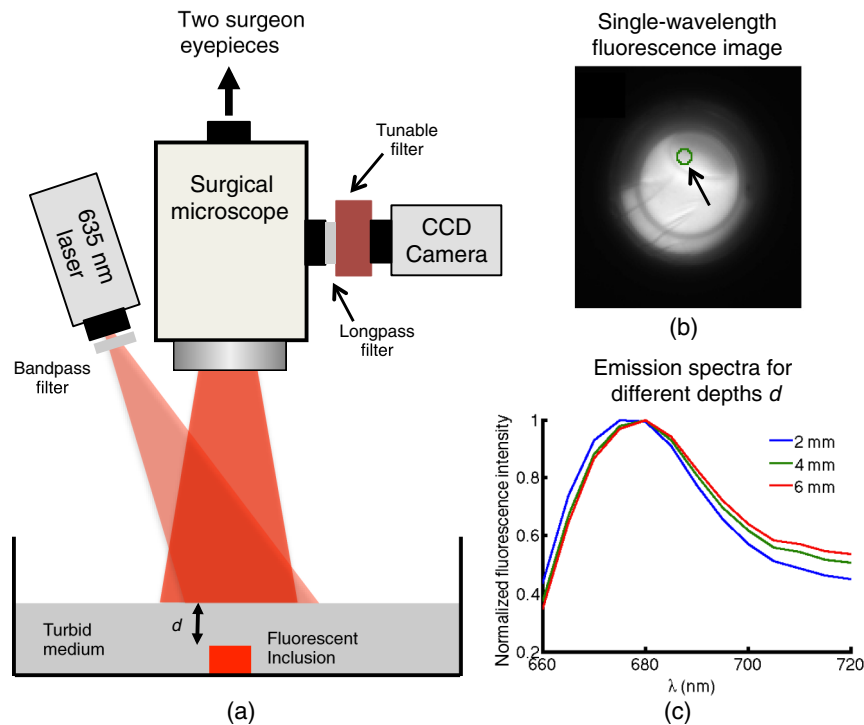


Fig. 1 (a) Schematics of the hyperspectral imaging system and the tissue-simulating phantom with a subsurface fluorescent inclusion. (b) Fluorescence image of the AF 647-filled inclusion at 670 nm at $d = 0$. (c) Representative fluorescence emission spectra collected within the circled area in the top right image for different depths, showing the measurable spectral distortions (normalized to the peak emission value).

detection system has been described elsewhere.⁵ In brief, it comprises a liquid crystal tunable filter (LCTF-VariSpec, CRi), a 650-nm long-pass filter (Chroma), and a charge-coupled device camera (PixelFlyUSB, PCO). The detection subassembly is attached to the side port using a custom optical adapter (TrueTex), ensuring that the magnification and FOV of the fluorescent images are consistent with what the surgeon views through the microscope eyepieces. A long-pass filter (>5 OD attenuation above 635 nm) blocks most of the excitation light, while the liquid crystal tunable filter then selects the fluorescence detection wavelength in 5 nm increments from 650 to 720 nm, allowing the acquisition of 14 fluorescence images at different wavelengths. For fluorescence excitation, the light from a 635-nm laser diode (Intense Co) with ~270-mW maximum power is guided through a collimator and a 635 ± 10 -nm band-pass filter (Chroma) to eliminate out-of-peak background light. At each fluorescence detection wavelength, a diffuse reflectance image is also acquired with the long-pass filter removed to allow the acquisition of 14 reflectance images at different wavelengths.

2.2 Tissue-Simulating Phantom Studies

A phantom (Fig. 1) was designed to simulate a discrete fluorescent tumor surrounded by tissue with minimal autofluorescence. It comprised a 20-cm diameter black plastic cylindrical container filled with intralipid (Patterson Veterinary Supply) for light scattering and bovine methemoglobin (Sigma Aldrich) for absorption, each at different concentrations to provide a range of optical properties consistent with normal brain tissue at 700 nm: $\mu_s' = 23 \text{ cm}^{-1}$ (1 part intralipid 20% to 10 parts water) for the first two phantoms and $\mu_s' = 31 \text{ cm}^{-1}$

(1.36 parts intralipid 20% to 10 parts water) for the third phantom; $\mu_a = 0.05 \text{ cm}^{-1}$ (2 mg/ml mHb) for the first phantom and $\mu_a = 0.07 \text{ cm}^{-1}$ (2.5 mg/ml) for the second and third phantoms: see Table 1.

A 1-cm diameter, 1-cm high transparent hollow inclusion was placed at the center of the larger container described above. The smaller inclusion was filled with a solution composed of 1 $\mu\text{g/ml}$ of the fluorophore Alexa Fluor 647 (Life Technologies) mixed with the same intralipid/methemoglobin solutions used for the turbid medium material surrounding the inclusion. The subsurface depth, d , to the top of the inclusion (from the surface of the liquid) was increased in 1 mm steps until the fluorescence signal was indistinguishable from the nonspecific background (at $d > 6$ mm in all cases) of the residual excitation light bleed through and intrinsic fluorescence of the intralipid. For repeatability and to minimize the impact of

Table 1 Optical properties (at 670 nm in cm^{-1}) used for the experimental studies and single-point depth recovery results (all in mm) associated with the three different techniques.

Optical properties		Technique 1		Technique 2		Technique 3	
μ_s' (cm^{-1})	Hb (mg/mL)	Mean error	Max error	Mean error	Max error	Mean error	Max error
23	2.0	-0.2	0.4	1.1	1.5	-0.4	0.7
23	2.5	-1.3	1.8	0.2	0.4	-1.0	1.5
31	2.5	-0.9	1.3	-0.5	1.1	-0.8	1.2

time on tissue phantom properties, the experiments in this work were conducted with a dye (Alexa Fluor 647) having more favorable biochemical properties than PpIX (e.g., quantum yield and photostability) but having similar spectral features when excited with red light. The incident fluorescence excitation power density was 20 mW/cm² over a circular FOV of 24 cm² for a distance of 20 cm between the microscope condenser lens and the phantom surface. The total image acquisition time (14 fluorescence images and 14 reflectance images) was in all cases <10 s. In order to account for the instrument response function of the imaging system, each reflectance image was normalized to the corresponding image taken using a Spectralon diffuse reflectance standard (Labsphere).

2.3 Monte Carlo Simulations

Monte Carlo simulations were performed using a plug-in developed for the GEANT4/GAMOS radiation transport model.³⁶ The input optical properties included those used in the phantom measurements, and additional absorption-scattering combinations were included to verify that the results were valid over a broader range of optical properties (Table 2). Each simulation launched 10⁸ photons in a 20-cm diameter uniform beam for each inclusion depth and combination of optical properties. The quantum yield of PpIX was set at 0.004, while the diffuse reflectance measurements spanned 630 to 720 nm in 10 nm steps. The light intensity at the surface was recorded for both the fluorescence emission and the white-light diffuse reflectance. The simulated source of fluorescence was a 5-mm thick slab, where the depth from the top of the inclusion to the surface ranged from 0 to 10 mm in 1 mm steps.

3 Results

3.1 Single-Point Analysis: Comparison with Experimental Data

The average fluorescence spectra, F^λ , and diffuse reflectance spectra, R^λ , were evaluated over a 3 × 3 pixels region of interest

Table 2 Optical properties (at 670 nm in cm⁻¹) used for the Monte Carlo light transport studies and single-point depth recovery results (all in mm) associated with the three different techniques.

Optical properties		Technique 1		Technique 2		Technique 3	
μ_s' (cm ⁻¹)	Hb (mg/mL)	Mean error	Max error	Mean error	Max error	Mean error	Max error
21	0.4	1.3	1.5	-1.1	1.6	-2.2	3.3
21	2.0	-0.1	0.8	-0.3	0.6	-1.8	2.7
21	4.0	-0.5	1.8	-0.1	1.5	-1.6	2.9
11	0.4	1.7	2.4	-0.8	1.1	-3.0	4.4
11	2.0	-0.2	0.7	-1.0	1.5	-3.4	4.4
11	4.0	0.0	1.1	0.1	0.9	-2.7	4.3
23	2.0	-0.2	0.6	0.8	1.9	-0.8	1.1
23	2.5	-0.3	1.0	0.8	1.9	-0.8	1.4
31	2.5	-0.4	1.8	0.8	1.8	0.4	1.1

close to the middle of the inclusion, as indicated by the circle in Fig. 1(b). A MATLAB® script (MathWorks) was developed to calculate the corresponding dual-wavelength fluorescence ratios (DWFR) for all wavelength pairs and for each inclusion depth, $d = 0$ to 6 mm, within the region of interest,

$$\Gamma^d = \frac{F^{\lambda_i}}{F^{\lambda_j}}, \quad (6)$$

where the indices i and j are running from 1 to 14, i.e., over all spectral bands (wavelengths) detected with the imaging system. The DWFR at each depth, d , was then divided by the DWFR value at $d = 0$ mm. Using Eq. (4) and the mathematical identity $\ln(a/b) = \ln(a) - \ln(b)$, it is seen that normalizing by the $d = 0$ mm image accomplishes three things: (1) it isolates the depth-dependent part of the fluorescence ratio independent of the emission spectrum of the dye, (2) it corrects for the wavelength-dependent system response, and (3) it removes the dependence on the parameter b found in Eq. (4):

$$\ln(\Gamma_N^d) = \ln\left(\frac{\Gamma^d}{\Gamma_{d=0}^d}\right) = m \times d. \quad (7)$$

Then, under the hypothesis that Eq. (1) captures the essential light transport processes, the fluorophore depth can be estimated by dividing the logarithm of the normalized DWFR in Eq. (7) by m , which is computed as described below. However, depth retrieval based on Eq. (7) requires that a fluorescence ratio measurement be made for $d = 0$ mm, which amounts to making a reference measurement of the fluorophore of interest (AF 647 in the present study). In practice, this could be achieved (e.g., during a fluorescence-guided surgery procedure) by using a fluorescence ratio measurement made on cancer tissue located directly on the surface of the surgical cavity.

As a result of Eq. (7), it is found that depth retrieval relies on the ability to: (1) acquire zero-depth data (for calibration purposes through normalization) corresponding to a reference measurement made with no intervening tissue between the imaging system and a standard Alexa Fluor 647 fluorescence source and (2) compute m . Table 3 summarizes the three techniques investigated to compute m , including the mathematical expressions used and the required input parameters. Each technique is now briefly described: Technique 1 (diffusion equation solution) is diffusion model based and requires both tissue absorption and reduced scattering coefficients to be known *a priori*, with m then being directly computed using Eq. (1). The other two techniques were designed to estimate m with a minimum number of input parameters. For Technique 3 (non-model based), since diffusion modeling¹⁹ and experiments^{34,37} have shown that m is directly related to factors responsible for the differential tissue attenuation between λ_i and λ_j , we used empirical combinations of the measured diffuse reflectance values, R^λ in the bands around λ_i and λ_j as a surrogate for tissue attenuation. Several mathematical expressions were considered (e.g., $(R_d^{\lambda_1} - R_d^{\lambda_2})/R_d^{\lambda_1}$, $\ln(R_d^{\lambda_1}/R_d^{\lambda_2})^x$ for a large range of x values), but the simple expression shown in Table 3 gave the most accurate predictions compared to the experimental phantom results and the Monte Carlo simulations. Technique 2 is a hybrid between Techniques 1 and 3. It is partly model based, since it does not require prior knowledge of the tissue absorption coefficient but does require the reduced scattering coefficient value at 700 nm as an input parameter. As with Technique 3,

Table 3 Main characteristics of the three different techniques used to recover depth.

Technique	Description	Input parameters	Limitations	m (mm ⁻¹)
1	Diffusion equation solution	μ_a, μ_s' , infinite medium boundary conditions	Absorption and reduced scattering needed	$m = \frac{1}{\delta^2} - \frac{1}{\delta^2_1}$
2	Empirical scattering correction	μ_s'	Reduced scattering needed	$m = \ln\left(\frac{R_d^{\lambda_1}}{R_d^{\lambda_2}}\right) \cdot \frac{\mu_s'(700\text{nm})}{3.28}$
3	Non-model based	None	Not accurate for all sets of optical properties	$m = \ln\left(\frac{R_d^{\lambda_1}}{R_d^{\lambda_2}}\right)$

the expression shown in Table 3 for Technique 2 was found through an optimization process. In cases where the calculation of the parameter m requires the optical properties as input values, the known optical properties of the tissue phantom were used (see Sec. 2.2).

For conciseness, the results for the representative wavelength pair 670 and 720 nm are presented here. However, Eq. (7) and fluorescence ratio measurements were used to predict depth using other wavelength pairs (one wavelength pair at the time and not by using the information of several wavelength pairs simultaneously) since the imaging system is acquiring spectroscopic data for every camera pixel. The results for other wavelength pairs are discussed in the Discussion section. Figures 2 and 3 show the results (based on the three techniques in Table 3) for two different sets of optical properties and where depth predictions are made based on the experimental data for a fluorescent inclusion. In Figs. 2(a) and 3(a), the points associated with the label “Experimental” are the DWFR values computed with the experimental data. Figures 2(b) and 3(b) show the graphs of the predicted depths (d_p) computed using Eq. (7) for all three techniques as a function of true depth values (d_t), i.e., the actual distance between the top of the fluorescent inclusion and the surface of the bulk medium in the experimental phantom (Fig. 1). On those graphs, the straight line is plotted for reference and simply represents the real depth values. Figures 2(c) and

3(c) and (d) present the experimental errors (absolute and relative) associated with depth predictions when compared with the real depths. Table 1 shows the corresponding differences between the calculated and true depths (mean and maximum errors) for all sets of optical properties and all three techniques.

3.2 Wide-Field Topographic Maps: Comparison with Experimental Data

The same experimental dataset as used in Sec. 3.1 was used to retrieve the fluorophore depth across the full FOV of the camera using fluorescence ratio measurements for the wavelength pair 670 and 720 nm. A topographic map was produced using Eq. (7) to predict local depth values using the three techniques in Table 3. The reference fluorescence ratio measurement used in the equation was the fluorescence ratio measured directly at the center of the $d = 0$ mm fluorescence images. For the 670 and 720-nm wavelength pair image, pixels were binned to increase the signal to noise such that the spatial resolution was ~ 1 mm, and pixels were retained only above a fluorescence intensity threshold corresponding to $\geq 50\%$ of the highest intensity of the 670-nm fluorescence image. In fact, pixels below this threshold did not lead to physically meaningful depth values and the corresponding raw spectra typically did not show the spectral features of Alexa Fluor 647. Pixels with insufficient signal to

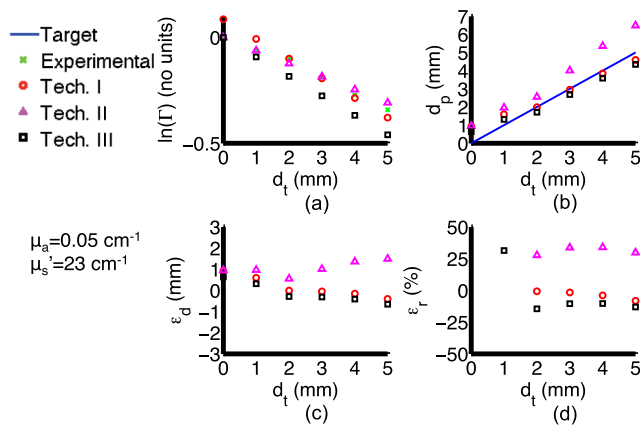


Fig. 2 Comparison of single-point estimation with the experimental phantom measurements at 670 nm using the bulk optical properties $\mu_a = 0.05 \text{ cm}^{-1}$ and $\mu_s' = 23 \text{ cm}^{-1}$: (a) Dual-wavelength fluorescence ratios (DWFR) as a function of the true depth d_t . (b) Depth estimation using the three different techniques versus the true depth, with the line representing $d_p = d_t$, where d_p is the estimated depth. (c) Error in absolute depth estimate (ϵ_d). (d) Relative error in depth estimate (ϵ_r). “Experimental” points only appear in (a), which shows the experimentally measured values for the DWFR.

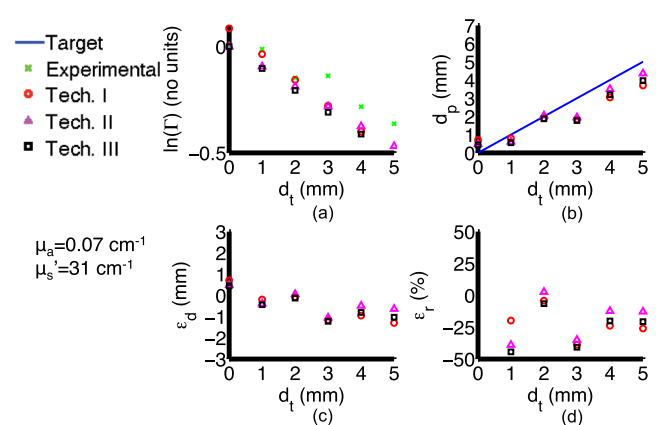


Fig. 3 Comparison of single-point estimation with the experimental phantom measurements at 670 nm using the bulk optical properties $\mu_a = 0.07 \text{ cm}^{-1}$ and $\mu_s' = 31 \text{ cm}^{-1}$: (a) Dual-wavelength fluorescence ratios (DWFR) as a function of the true depth d_t . (b) Depth estimation using the three different techniques versus the true depth, with the line representing $d_p = d_t$, where d_p is the estimated depth. (c) Error in absolute depth estimate (ϵ_d). (d) Relative error in depth estimate (ϵ_r). “Experimental” points only appear in (a), which shows the experimentally measured values for the DWFR.

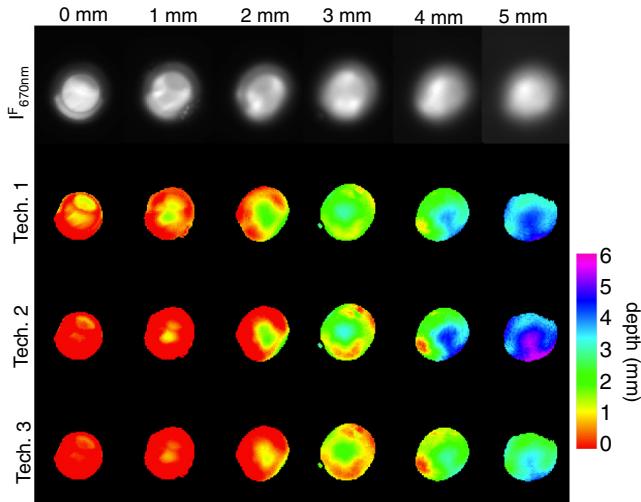


Fig. 4 Topographic maps recovered using Eq. (7) with the three proposed techniques (see Table 3) for the bulk optical properties $\mu_a = 0.05 \text{ cm}^{-1}$ and $\mu_s' = 23 \text{ cm}^{-1}$ at 670 nm. The true depth (from $d_t = 0$ to 5 mm) of the fluorescent inclusion is indicated and the color bar represents the recovered depths. The top row of images show the raw measured fluorescence at 670 nm.

noise or non dye-specific signals are represented with the color black in Fig. 4. The figure only shows representative results for $\mu_a = 0.05 \text{ cm}^{-1}$ and $\mu_s' = 23 \text{ cm}^{-1}$, but similar images were obtained for the other optical properties considered.

3.3 Single-Point Analysis: Comparison with Monte Carlo Data

In order to validate the experimental results and extend the range of optical properties considered, detailed numerical simulations were carried out over a range of tissue properties relevant for brain imaging. For conciseness, in Figs. 5 and 6 and in Table 2, we show only the results for the representative wavelength pair 670 nm and 720 nm. Table 2 shows recovered depth accuracy figures (mean, standard deviation, and maximum and

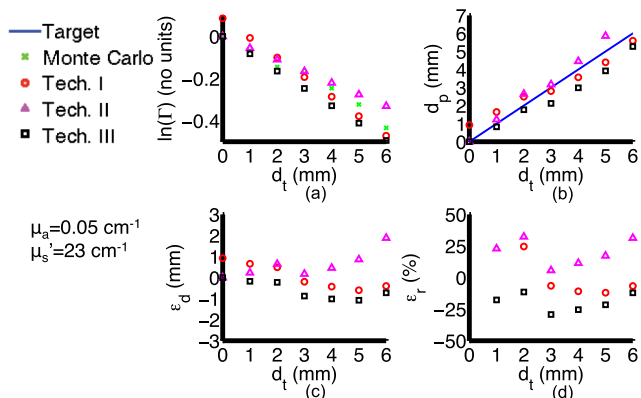


Fig. 5 Comparison of single-point estimation with Monte Carlo simulations for bulk optical properties $\mu_a = 0.05 \text{ cm}^{-1}$ and $\mu_s' = 23 \text{ cm}^{-1}$: (a) Dual-wavelength fluorescence ratios (DWFR) as a function of the true depth d_t . (b) Depth estimation using the three different techniques versus the true depth, with the line representing $d_p = d_t$, where d_p is the estimated depth. (c) Error in absolute depth estimate (ϵ_d). (d) Relative error in depth estimate (ϵ_r). “Monte Carlo” points only appear in (a), which shows the simulated values for the DWFR.

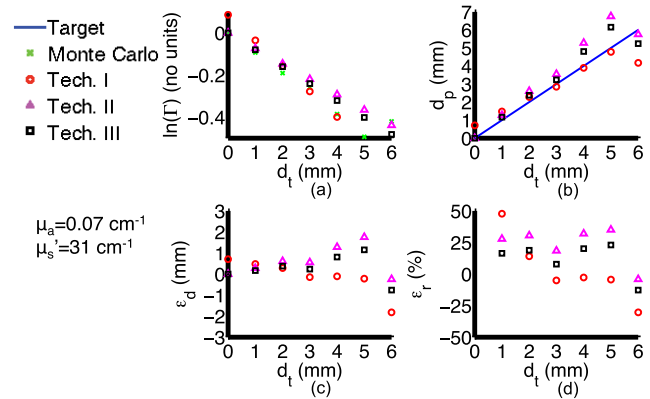


Fig. 6 Comparison of single-point estimation with Monte Carlo simulations for bulk optical properties $\mu_a = 0.07 \text{ cm}^{-1}$ and $\mu_s' = 31 \text{ cm}^{-1}$: (a) Dual-wavelength fluorescence ratios (DWFR) as a function of the true depth d_t . (b) Depth estimation using the three different techniques versus the true depth, with the line representing $d_p = d_t$, where d_p is the estimated depth. (c) Error in absolute depth estimate (ϵ_d). (d) Relative error in depth estimate (ϵ_r). “Monte Carlo” points only appear in (a), which shows the simulated values for the DWFR.

minimum errors) for all sets of optical properties considered using the techniques in Table 3. The predictions (fluorescence ratio and recovered depth) made with Techniques 1 and 2 verify the Monte Carlo simulated data for all sets of optical properties. However, we find that Technique 3 is uniquely suited for optical properties having the lowest values of scattering.

4 Discussion

The Monte Carlo simulations (in single-point analysis mode only) show that, for optical properties consistent with brain tissue, Technique 1 (tissue input parameters to compute m : absorption and reduced scattering) and Technique 2 (input tissue parameter to compute m : reduced scattering only) are both able to accurately recover the fluorophore depth up to 5 mm with an average error of ± 1 mm, while the depth errors with Technique 3 (no tissue input parameters to compute m) were on average ± 1.5 mm. The single-point experimental data were consistent with these findings. Although experimental and Monte Carlo data were acquired for multiple wavelengths, the fluorescence ratio results were only presented above for the wavelength pair 670 and 720 nm. However, detailed analyses for all possible wavelength pairs (considered one pair at the time for topographic depth recovery) led to similar conclusions, while, in general, using both wavelengths above 700 nm resulted in larger errors, likely due to the smaller spectroscopic changes in hemoglobin absorption in that region. As might be expected, maximizing m and achieving the best agreement with the models were obtained using wavelength pairs associated with the largest relative changes in tissue optical properties. Simulations for a slab rather than a finite-size inclusion were presented here in order to evaluate the technique using datasets where the main variable is depth and not the actual geometry of the fluorescent source. However, Monte Carlo simulations were also performed for a geometry identical to that used for the experimental work, i.e., a cylindrical inclusion. Although the results for a cylindrical inclusion are not presented here for conciseness, they have led to single-point analysis results essentially identical to those described in Sec. 3.3.

Depth recovery based on experimental data was also topographically achieved (Fig. 4) using the full wide-field optical datasets. In general, for all three techniques, the recovered depth was underestimated by ~ 0.8 mm and the resulting images are not homogenous across the entire field. This may be due to several experimental and model-related factors, including edge effects of the inclusion such as seen on the raw fluorescence image in Fig. 1(b). Experimental factors resulting in depth inaccuracies might also include a slight unmixing of intralipid and hemoglobin, possible spatial variations in the light source, stochastic noise propagating into the radiometric measurements, the intralipid autofluorescence background and the approximations in Eq. (1) that the fluorescence source is point-like and embedded in an infinite, optically homogeneous diffusive medium. Some of these inaccuracies perhaps speak more to the difficulty of creating representative phantoms rather than the validity of the technique. The precision of depth recovery can be improved by (1) maximizing the signal to noise in the single-wavelength fluorescence images and (2) ensuring that the tissue optical properties are known with high accuracy so that Technique 1 can be used. In addition, (3) the spectral shape of nonspecific fluorescent sources is usually known and could be deconvoluted from that associated with the dye of interest in order to minimize the impact of tissue autofluorescence.

With the current system, wide-field data acquisition requires <10 s for all the fluorescent source depths and tissue optical properties considered (each time, 14 fluorescence images and 14 reflectance images are detected). While this integration time is suboptimal for surgical applications, the critical result shown here is that as few as two fluorescence wavelengths are required for topographic imaging, which should reduce the total imaging to <1 s, and potentially much lower when using commercially available faster and more sensitive cameras. Beyond speed and instrument simplicity, one key advantage of this technique is that the ratio of fluorescence intensity at two wavelengths is self-calibrating in that it decouples the molecular information (fluorophore quantum yield, concentration, and lifetime) from the fluorophore spatial localization, as detailed in Ref. 19. This is important because of the difficulty in diffuse tomography to accurately reconstruct and separate optical contrast, spatial localization, and volume.

As mentioned in Sec 2.2, the experimental phantom results presented here suggest that the autofluorescence of the bulk medium surrounding the fluorescent inclusion is sufficiently high to prevent detection for depths >6 mm. However, the actual maximum detectable depth of the proposed technique when using ALA-PpIX for surgical guidance will be subsequently determined in the scope of a clinical study where the technique is used for glioma patients. As previously reported,^{6,13} the signal-to-background ratio for ALA-PpIX guided brain surgery, at least for high-grade glioma and meningioma, is high enough that the impact of tissue autofluorescence should be negligible. However, for cases where the concentrations of PpIX are much smaller (possibly in the diffusely cancer-infiltrated boundaries of the tumor that are undetectable with the existing technologies), it may be necessary to properly subtract the autofluorescence background from the PpIX signals, and thus increase the maximum detectable depth. A technique using a spectral unmixing algorithm to separate the spectral contribution of autofluorescence from that of the fluorophore of interest is currently being developed by our group. We are also pursuing the use of hyperspectral spatial light modulation

imaging¹⁸ in order to map the tissue optical properties to retrieve tissue optical properties for every imaging pixel in real time. These optical properties will be used to compute m using the analytic expression in Eq. (1)—and retrieve depth using Eq. (7). We and other groups^{26,27} are also actively investigating fluorophores at longer NIR wavelengths in order to increase the effective depth of subsurface fluorophore detection, so it can be expected that the current depth limit with PpIX can be further improved. However, the requirement for tumor specificity of the fluorescent probe remains and it may be difficult to improve on or even match that of ALA-PpIX.

As demonstrated here, an approach to estimating the depth of subsurface fluorescence has been directly implemented on a commercial neurosurgical microscope, making it suitable for clinical application. This is in contradiction to other optical tomography techniques that may be difficult to seamlessly integrate into the neurosurgical workflow because they are relying, e.g., on raster-scanning techniques and are often based on data types extracted from frequency-modulated and time-resolved signals. The simplicity of the proposed approach is that it relies on the acquisition of wide-field continuous-wave images at two different wavelengths. As a result, data acquisition with our technique can be more rapid (compared to other optical tomography techniques) since only two planar fluorescence images are required to provide depth values with minimal data processing time. In fact, the data processing required to obtain pixelized depth values can be almost instantaneous and does not require, e.g., the creation of a finite-elements mesh and the reconstruction of images based on the resolution of an inverse problem. However, the disadvantage of our topography technique is that the resulting depth estimates might be less precise as those that would be obtained using an epi-illumination tomography technique, especially close to the edges of the sources of optical contrast where the use of multiple projections could be required in order to more accurately localize fluorescent objects. It should be noted that providing neurosurgeons with even an approximate depth of tumor lying below the surface of the resection bed is critical to enable maximal safe resection in order to improve patient outcomes, since even small amounts of residual tumor can have a marked impact on the efficacy of adjuvant therapies and consequent survival.^{7,8} In fact, even the dichotomic information of whether or not the information relating to a source of fluorescence is on the surface or underneath the surface would be of high value to neurosurgeons.

Acknowledgments

This work was supported by US National Institutes of Health (US) under Grants No. R01NS052274-01A2 and K25 CA164248-01 (CCK) and NSERC (Canada) Discovery Grant Program.

References

1. A. L. Vahrmeijer et al., "Image-guided cancer surgery using near-infrared fluorescence," *Nat. Rev. Clin. Oncol.* **10**(9), 507–518 (2013).
2. T. J. Snoeks et al., "Towards a successful clinical implementation of fluorescence-guided surgery," *Mol. Imaging Biol.* **16**(2), 147–151 (2014).
3. U. Pichlmeier et al., "Resection and survival in glioblastoma multiforme: an RTOG recursive partitioning analysis of ALA study patients," *Neuro. Oncol.* **10**(6), 1025–1034 (2008).
4. W. Stummer et al., "Fluorescence-guided surgery with 5-aminolevulinic acid for resection of malignant glioma: a randomised controlled multicentre phase III trial," *Lancet Oncol.* **7**(5), 392–401 (2006).

5. P. A. Valdes et al., "Quantitative, spectrally-resolved intraoperative fluorescence imaging," *Sci. Rep.* **2**, 798 (2012).
6. P. A. Valdes et al., "Quantitative fluorescence in intracranial tumor: implications for ALA-induced PpIX as an intraoperative biomarker," *J. Neurosurg.* **115**(1), 11–17 (2011).
7. W. Stummer et al., "Prospective cohort study of radiotherapy with concomitant and adjuvant temozolomide chemotherapy for glioblastoma patients with no or minimal residual enhancing tumor load after surgery," *J. Neurooncol.* **108**(1), 89–97 (2012).
8. M. J. McGirt et al., "Extent of surgical resection is independently associated with survival in patients with hemispheric infiltrating low-grade gliomas," *Neurosurgery* **63**(4), 700–707 (2008).
9. P. A. Valdes et al., "202 5-aminolevulinic acid-induced protoporphyrin IX fluorescence in low-grade gliomas," *Neurosurgery* **61**(Suppl 1), 227–228 (2014).
10. P. A. Valdes et al., "5-Aminolevulinic acid-induced protoporphyrin IX fluorescence in meningioma: qualitative and quantitative measurements in vivo," *Neurosurgery* **10**(Suppl 1), 74–82 (2014).
11. D. W. Roberts et al., "Adjuncts for maximizing resection: 5-aminolevulinic acid," *Clin. Neurosurg.* **59**, 75–78 (2012).
12. P. A. Valdes et al., "A spectrally constrained dual-band normalization technique for protoporphyrin IX quantification in fluorescence-guided surgery," *Opt. Lett.* **37**(11), 1817–1819 (2012).
13. P. A. Valdes et al., "Combined fluorescence and reflectance spectroscopy for *in vivo* quantification of cancer biomarkers in low- and high-grade glioma surgery," *J. Biomed. Opt.* **16**(11), 116007 (2011).
14. K. Bekelis et al., "Quantitative and qualitative 5-aminolevulinic acid-induced protoporphyrin IX fluorescence in skull base meningiomas," *Neurosurg. Focus* **30**(5), E8 (2011).
15. A. Kim et al., "Quantification of *in vivo* fluorescence decoupled from the effects of tissue optical properties using fiber-optic spectroscopy measurements," *J. Biomed. Opt.* **15**(6), 067006 (2010).
16. A. Kim et al., "A fiberoptic reflectance probe with multiple source-collector separations to increase the dynamic range of derived tissue optical absorption and scattering coefficients," *Opt. Express* **18**(6), 5580–5594 (2010).
17. P. A. Valdes et al., "System and methods for wide-field quantitative fluorescence imaging during neurosurgery," *Opt. Lett.* **38**(15), 2786–2788 (2013).
18. S. D. Konecky et al., "Spatial frequency domain tomography of protoporphyrin IX fluorescence in preclinical glioma models," *J. Biomed. Opt.* **17**(5), 056008 (2012).
19. F. Leblond et al., "Analytic expression of fluorescence ratio detection correlates with depth in multi-spectral sub-surface imaging," *Phys. Med. Biol.* **56**(21), 6823–6837 (2011).
20. P. A. Valdes et al., "Gadolinium- and 5-aminolevulinic acid-induced protoporphyrin IX levels in human gliomas: an *ex vivo* quantitative study to correlate protoporphyrin IX levels and blood-brain barrier breakdown," *J. Neuropathol. Exp. Neurol.* **71**(9), 806–813 (2012).
21. A. Kim et al., "Topographic mapping of subsurface fluorescent structures in tissue using multiwavelength excitation," *J. Biomed. Opt.* **15**(6), 066026 (2010).
22. W. Stummer and M. A. Kamp, "The importance of surgical resection in malignant glioma," *Curr. Opin. Neurol.* **22**(6), 645–649 (2009).
23. M. Lacroix et al., "A multivariate analysis of 416 patients with glioblastoma multiforme: prognosis, extent of resection, and survival," *J. Neurosurg.* **95**(2), 190–198 (2001).
24. J. S. Smith et al., "Role of extent of resection in the long-term outcome of low-grade hemispheric gliomas," *J. Clin. Oncol.* **26**(8), 1338–1345 (2008).
25. S. Achilefu, "Introduction to concepts and strategies for molecular imaging," *Chem. Rev.* **110**(5), 2575–2578 (2010).
26. S. Achilefu, "The insatiable quest for near-infrared fluorescent probes for molecular imaging," *Angew. Chem. Int. Ed. Engl.* **49**(51), 9816–9818 (2010).
27. X. Zhang et al., "Near-infrared molecular probes for *in vivo* imaging," *Curr. Protoc. Cytom.* Chapter 12, Unit 12.27 (2012).
28. F. Leblond et al., "Pre-clinical whole-body fluorescence imaging: review of instruments, methods and applications," *J. Photochem. Photobiol. B* **98**(1), 77–94 (2010).
29. K. M. Tichauer et al., "Imaging workflow and calibration for CT-guided time-domain fluorescence tomography," *Biomed. Opt. Express* **2**(11), 3021–3036 (2011).
30. R. W. Holt et al., "Multiple-gate time domain diffuse fluorescence tomography allows more sparse tissue sampling without compromising image quality," *Opt. Lett.* **37**(13), 2559–2561 (2012).
31. A. Laidevant et al., "Analytical method for localizing a fluorescent inclusion in a turbid medium," *Appl. Opt.* **46**(11), 2131–2137 (2007).
32. B. Yuan and Q. Zhu, "Separately reconstructing the structural and functional parameters of a fluorescent inclusion embedded in a turbid medium," *Opt. Express* **14**(16), 7172–7187 (2006).
33. D. Hall et al., "Simple time-domain optical method for estimating the depth and concentration of a fluorescent inclusion in a turbid medium," *Opt. Lett.* **29**(19), 2258–2260 (2004).
34. J. Swartling et al., "Fluorescence spectra provide information on the depth of fluorescent lesions in tissue," *Appl. Opt.* **44**(10), 1934–1941 (2005).
35. S. L. Jacques and B. W. Pogue, "Tutorial on diffuse light transport," *J. Biomed. Opt.* **13**(4), 041302 (2008).
36. A. K. Glaser et al., "A GAMOS plug-in for GEANT4 based Monte Carlo simulation of radiation-induced light transport in biological media," *Biomed. Opt. Express* **4**(5), 741–759 (2013).
37. A. Pifferi et al., "Performance assessment of photon migration instruments: the MEDPHOT protocol," *Appl. Opt.* **44**(11), 2104–2114 (2005).

Biographies of the authors are not available.